

# Vortex shedding and frequency selection in flapping flight

By Z. JANE WANG†

Courant Institute of Mathematical Sciences, New York University, NY 10012, USA

(Received 26 October 1998 and in revised form 15 November 1999)

Motivated by our interest in unsteady aerodynamics of insect flight, we devise a computational tool to solve the Navier–Stokes equation around a two-dimensional moving wing, which mimics biological locomotion. The focus of the present work is frequency selection in forward flapping flight. We investigate the time scales associated with the shedding of the trailing- and leading-edge vortices, as well as the corresponding time-dependent forces. We present a generic mechanism of the frequency selection as a result of unsteady aerodynamics.

---

## 1. Introduction

Flapping motion is a basic mode of locomotion in insects, birds, and fish. Thrust and lift are generated as a result of interactions between flapping wings or tails and their surrounding fluids. Despite a long-standing tradition in scientific work inspired by biological locomotion, which at least dates back to the 1500s when Leonardo da Vinci designed a number of ornithopters based on bird flight, the highly unsteady nature of flows around a flapping wing make the theoretical and experimental treatment of the subject difficult, and our partial understanding of the vortex shedding in unsteady flows, which is crucial to the force generation, is far from satisfactory. Pioneering work in the biofluidynamics of animal locomotion in the quasi-steady limit was done by Weis-Fogh & Jensen (1956), Lighthill (1975), among others. Comprehensive reviews of much previous work can be found in the articles by Lighthill (1970), Maxworthy (1981), Ellington (1984), and Spedding, (1992). Some recent experimental work can be found in Ellington *et al.* (1996) and Dickenson, Lehmann & Sane (1999).

We note that a distinct feature of biological flight and swimming is the frequency variation among different species and within each species, which cannot be entirely accidental. Even to a layman's eye, there is a consistent trend in these variations: large animals, birds and fish, appear to operate in the lower frequency regime, while the smaller ones, insects, in the higher frequency regime.

An insect, bird or fish has a huge parameter space at its disposal, which includes the mechanical properties of wings and muscles, as well as the dynamics of the wing. The selected frequency must be a result of the combined effects of biology and physics. In the past, the dependence of frequency on size has been estimated using dimensional arguments related to power consumption (Lighthill 1977; Weis-Fogh 1977; Wu 1977). It has also been argued that the flapping frequency is dictated by the natural oscillation frequency of the muscles (Greenewalt 1962). In this work, we

† Permanent address: Theoretical and Applied Mechanics, Cornell University, Ithaca, NY 14853, USA; email: jane.wang@cornell.edu.

instead focus on the role of the unsteady aerodynamics and ask whether and how aerodynamics might select a range of preferred frequencies.

To separate the biology from this complex problem, we choose to study a two-dimensional flapping wing at Reynolds numbers in the range of insect flight. Despite the simplicity of the model, the unsteady effects of complex vortical flows around a flapping wing, and the corresponding forces, are not fully understood. In particular, it is unclear how the intrinsic time scales in unsteady flows can play a role in force generation.

The basic mechanism of thrust generation in flapping flight was illustrated long ago by Glauert (1929) in a classical linear theory of an oscillating wing in inviscid flow. Glauert's theory predicts a thrust, generated by shedding a vortex wake, which carries the momentum backward with respect to the wing. For a fixed advance ratio, which measures the ratio of maximum flapping velocity to the mean forward velocity, Glauert's result predicts no preferred frequency, but rather, that the thrust coefficient  $C_t$  and the efficiency  $Q$  increase monotonically with decreasing frequency. This suggests a rather paradoxical situation: to achieve the best efficiency, birds or insects should flap at close to zero frequency.

More elaborate theories, including the vortex panel method and the unsteady lifting-line theory, have been developed for both bird flight (Phlips, East & Pratt 1981) and fish swimming (Lighthill 1970; Chopra 1976). These models again concluded that the thrust and efficiency depend on frequency monotonically. A more detailed review of various modelling methods can be found in Smith, Wilkin & Williams (1996).

Recently Hall, Pigott & Hall (1998) examined the power requirements for flapping flight. By applying a variational principle, they found a wake configuration which minimizes the induced power loss, a technique extended from the Betz criterion for optimal propellers. Their model showed optimal frequencies. This approach is computationally less expensive than solving the Navier–Stokes equation, because the wake solution is approximated by a two-dimensional vortex sheet and quasi-steady lift–drag relations are assumed. It would be worthwhile to compare such results with the ones obtained by direct numerical simulation.

Contrary to theories, experiments on oscillating foils have often shown the existence of 'optimal' parameters for a given experiment. For example, Triantafyllou, Triantafyllou & Gopalkrishnan (1991) showed that 'optimal' flapping occurs when the Strouhal number is in the range of 0.2–0.3. Their definition of the Strouhal number is equivalent to the advance ratio mentioned earlier. An optimal Strouhal number alone, however, does not select an optimal frequency, simply because one can vary frequency and amplitude simultaneously to fix the Strouhal number. In another experiment, Gursul & Ho (1992) examined the lift coefficient on a wing oscillating in the direction of the mean flow. They observed that the lift coefficient peaks at a certain frequency, and argued that this frequency could be related to the length scale of the leading-edge vortex. However, this leading-edge vortex alone does not fully explain why the thrust coefficient increases with the decreasing frequency before it decreases.

The purpose of our study is two-fold. First, we devise a computational tool to solve the Navier–Stokes equation around a two-dimensional moving wing, which is capable of mimicking biological locomotion. This then allows us to quantify the vortex dynamics and unsteady forces corresponding to different wing motions. Secondly, we apply such a tool to investigate the frequency selection mechanism in flapping flight, and reconcile the differences between the existing theories and experiments.

In addition to our interest in frequency selection in flapping flight, our computational tool is implemented in response to the general interest in quantifying the

dynamics of unsteady viscous vortical flows at intermediate-range Reynolds numbers, typically between  $10^2$  and  $10^4$ , and in the full range of frequency parameters. These computations can be especially useful in research on insect flight. Insects are different from large birds and fish in that they operate at relatively lower Reynolds numbers and higher frequency parameters. Consequently the applicability of inviscid quasi-steady analysis is questionable (Weis-Fogh & Jensen 1956; Ellington 1984; Norberg 1975; Childress 1981; Spedding 1993). Direct numerical simulation of unsteady viscous flows around a flapping wing would allow us to investigate the validity of the quasi-steady Kutta condition employed in previous theoretical models, as well as to suggest more realistic models of the dynamics of trailing- and leading-edge vortices. These computations can be further compared with experiments to cross-check the validity of different methods.

Ideally, three-dimensional computation around an elastic wing is desirable. Recently, Liu *et al.* (1998) applied a method of pseudo-compressibility to compute flows around a three-dimensional rigid wing, and examined the axial flows associated with the leading-edge vortex as seen in the experiments by Ellington *et al.* (Liu *et al.* 1998; Liu & Kawachi 1998; Ellington *et al.* 1996). However, from a practical point of view, while it is possible to resolve two-dimensional flows at Reynolds numbers relevant to insect flight, it remains to be seen whether one can do the same for three-dimensional flows. Therefore, a two-dimensional computation can serve both as a reliable tool in its own right and a useful reference point to be compared with three-dimensional simulation. Previously, Freymuth, Gustafson & Leben (1992) and Gustafson & Leben (1991) computed two-dimensional hovering flight. These results show qualitative agreement with the experiments. Their comparison of the forces, however, was inconclusive.

In our computation, we employ a high-order numerical scheme, an improvement over previous work, to resolve the vortex dynamics, which is crucial to the force generation on a moving wing. The computation described here serves as our basis of studies of forward and hovering flight. The latter will be reported in future publications.

In the present work, we focus on the question of frequency selection in forward flapping flight, as introduced at the beginning of this section. We investigate the time scales associated with the shedding of the trailing- and leading-edge vortices, as well as the corresponding forces. We present a generic mechanism of the frequency selection as a result of the unsteady aerodynamics.

In the next section, we define a flapping model and describe our computational method. The computational tool is tested by comparing results on impulsively started flows with analytical and experimental results (Bouard & Coutanceau 1980; Dickinson & Götz 1993). In §3 we show the existence of an optimal flapping sequence and signatures of the associated vorticity field. To unfold the basic mechanism behind the observed optimal, we investigate in detail the unsteady effects and the dynamics of the leading-edge vortex in an idealized single stroke. Finally we interpret optimal flapping with the help of our results on a single stroke, and confirm our findings with further numerical experiments. We conclude with a brief summary and comparisons of our results with existing literature on wing mechanics and animal flight.

## 2. Flapping model and computational method

We consider a simple model describing the forward flapping motions as drawn schematically in figure 1. The ellipse represents a wing element in the chord direction.

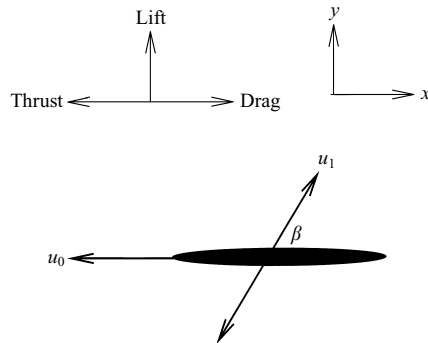


FIGURE 1. Flapping model. The ellipse represents a cross-section of a flapping wing in the chord direction. The thickness ratio is chosen to be 0.125 for most of our computations unless otherwise specified.  $u_0$  is the mean flight velocity,  $u_1$  the flapping velocity, and  $\beta$  the angle between the stroke plane and the  $x$ -axis. Mean thrust and lift are defined with respect to the direction of  $u_0$ .

The motion of the wing consists of the superposition of the mean forward motion, denoted by  $u_0$  and a sinusoidal flapping motion  $u_1(t)$ , in the direction of a line inclined at angle  $\beta$  to the horizontal, with an amplitude  $A$  and frequency  $f$ , i.e.  $u_1(t) = 2\pi f A \sin(2\pi f t)$ .

For simplicity, we choose the mean angle of attack to be zero, and set  $\beta$  to be  $\pi/2$ . We will discuss the effect of non-zero mean angle of attack at the end of the paper. The averaged resultant force in this case has only a horizontal component. In reality, insect and bird flight generate both lift and thrust by tilting the wing relative to the direction of flight.

The parameters,  $u_0$ ,  $f$ , and  $A$ , together with kinematic viscosity  $\nu$  and wing chord  $c$ , form three dimensionless quantities: the Reynolds number,  $Re$ , and the two Strouhal numbers,  $St_a$  and  $St_c$ , defined as:

$$Re = u_0 c / \nu, \quad (2.1)$$

$$St_a = f A / u_0, \quad (2.2)$$

$$St_c = f c / u_0, \quad (2.3)$$

Note that  $St_a$  measures the ratio of the maximum flapping velocity and the forward velocity, and  $St_c$  is the dimensionless flapping frequency. In the fluid mechanics literature, the Strouhal number is usually associated with the dimensionless shedding frequency of a von Kármán wake (Tritton 1992); here we use the term in a somewhat different context. In the insect flight literature  $St_a$  and  $St_c$  are sometimes referred to as the advance ratio and the reduced frequency parameter respectively. The flows around birds and insects can be considered incompressible: the Mach number is typically  $1/300$  and the frequency is about  $10\text{--}10^3$  Hz.

To solve the flows around a moving wing, we employ a fourth-order essentially compact finite difference scheme (EC4) for the incompressible Navier–Stokes equation developed by (E & Liu 1996). An advantage of the scheme is that at each time step, only two Poisson solvers are required to achieve a fourth order spatial accuracy. The scheme uses the vorticity-stream function formulation, and the vorticity boundary condition is explicitly enforced to satisfy the no-slip boundary condition. For a detailed description of the method see (E & Liu 1996).

In this study, in an effort to efficiently resolve the two-dimensional flow between  $Re = 10^2$  and  $Re = 10^4$ , we adapt the scheme to elliptic coordinates and treat the

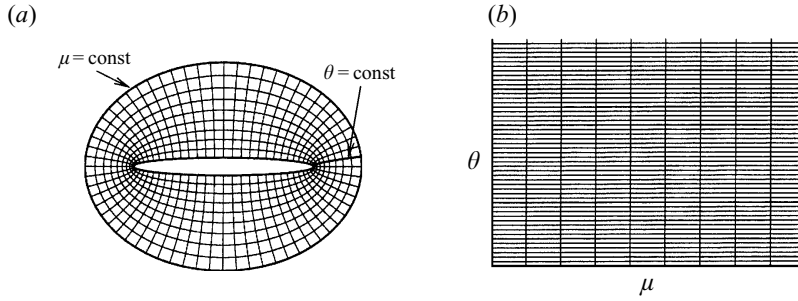


FIGURE 2. The elliptic coordinates  $(\mu, \theta)$  fitted to a two-dimensional wing. Confocal ellipses and hyperbolae correspond to constant  $\mu$  and  $\theta$ , respectively. The Cartesian coordinates, with periodic boundary conditions in the  $\theta$ -direction, conformally mapped from the elliptic coordinates.

far-field boundary condition on the stream function almost exactly in the Poisson solvers. The elliptic coordinates  $(\mu, \theta)$  are shown in figure 2, where constant  $\mu$  and  $\theta$  correspond to confocal ellipses and hyperbolae.

A uniform mesh in  $(\mu, \theta)$  is naturally clustered near the tips of the wing and is coarse at the far field in  $(x, y)$ -space. Such a grid is suitable for our problem since the vorticity is strongest near the tip of the ellipse and is weaker away from the body. Furthermore, the elliptic coordinates can be mapped onto a Cartesian coordinates via the conformal transformation:

$$x + iy = \cosh(\mu + i\theta), \quad (2.4)$$

which preserves the Laplacian up to a local scaling function  $S(\mu, \theta)$ :

$$\Delta_{x,y} = \Delta_{\mu,\theta}/S(\mu, \theta), \quad \text{with} \quad S(\mu, \theta) = \cosh^2 \mu - \cos^2 \theta. \quad (2.5)$$

The dimensionless Navier–Stokes equation for the two-dimensional vorticity field in the elliptic coordinates becomes

$$\frac{\partial(S\omega)}{\partial t} + (\sqrt{S}\mathbf{u} \cdot \nabla)\omega = \frac{1}{Re}\Delta\omega, \quad (2.6)$$

where  $\mathbf{u}$  is the velocity field,  $\omega$  the vorticity field, and  $Re$  the Reynolds number. For incompressible flows,  $\mathbf{u}$  and  $\omega$  can be expressed in terms of the stream function  $\Psi$ :

$$S\omega = \Delta\Psi, \quad (2.7)$$

$$\sqrt{S}\mathbf{u} = -\nabla \times \Psi, \quad (2.8)$$

where the derivatives are with respect to  $(\mu, \theta)$ . The conformal transformation results in a constant-coefficient Poisson equation for  $\Psi$ , which can be solved efficiently via FFT.

We solve the Navier–Stokes equation in the body-frame. For the translational motions considered here, no fictitious force appears in the vorticity equation. The no-slip boundary condition at the wing is enforced explicitly through the vorticity boundary condition at the boundary. The radius of the computational boundary is chosen to be 5 to 10 times the half-chord length. This large radius is affordable due to the stretched mesh in the elliptic coordinates. In the far field, the boundary condition on the stream function is given by the potential flow,

$$\Psi(r, \theta) = \Gamma \ln r + \sum_{n \geq 1} A_n \frac{e^{in\theta}}{r^n} \quad \text{for} \quad r > a, \quad (2.9)$$

where  $\Gamma$  is total circulation, and  $A_n$  the multipole moments of  $\omega$ . The correct solution can be obtained via an extra FFT to correct the solutions  $\tilde{\Psi}$  obtained with the approximate boundary condition  $\tilde{\Psi}(R, \theta) = \Gamma \ln R$ , where  $R$  is the radius at the computational boundary. The details are described in Wang (1999).

We use a fourth-order Runge–Kutta scheme for the time iterations, which exhibits a stability domain for this explicit scheme. The stability condition includes two CFL-like conditions related to the convection and diffusion time scales over a mesh size:

$$dt_1 = C_1 ds^2 \sinh^2 \mu_0 / 4\nu, \quad dt_2 = C_2 ds \sinh \mu_0, \quad (2.10)$$

where  $ds = \min(d\mu, d\theta)$ ,  $\mu = \mu_0$  at the ellipse, and  $C_1 = C_2 = 0.8$ . The time step is  $\min(dt_1, dt_2)$ . The basic time iteration in each computation step involves the following sequence:  $\omega^n \rightarrow \Psi^{n+1} \rightarrow \mathbf{u}^{n+1} \rightarrow \omega^{n+1}$ , where superscripts indicate the time step.

To resolve the flow, we keep at least 10 grid points along the radial direction in the boundary layer, and at least 30 points in the azimuthal direction around each tip, whose length scale is estimated by its radius of curvature. The typical resolution for  $Re \sim 1000$  is  $128 \times 256$  for single strokes, and  $256 \times 256$  for the flapping motion.

To test our code, we compute flow past a cylinder, a limiting case of an ellipse, and compare the results with experiments by Bouard & Coutanceau (1980). We find good agreement in the separation angle, as well as the velocity field as a function of time and space. As an additional check, we also compare the computed flow outside the boundary layer at early time with the potential solution. Both checks are detailed in the Appendix. In the next section, we will also compare the force measurements in a single stroke with the experiments by Dickinson & Götz (1993).

The forces on the ellipse can be computed from the vorticity field. In particular, the pressure force  $\mathbf{F}_p$  is determined by the vorticity flux, and the viscous force  $\mathbf{F}_v$  by the vorticity along the ellipse. More specifically,

$$\mathbf{F}_p = \rho\nu \int \frac{\partial \omega}{\partial \mu} (\sinh \mu_0 \sin \theta \hat{\mathbf{x}} + \cosh \mu_0 \cos \theta \hat{\mathbf{y}}) d\theta, \quad (2.11)$$

$$\mathbf{F}_v = \rho\nu \int \omega (-\cosh \mu_0 \sin \theta \hat{\mathbf{x}} + \sinh \mu_0 \cos \theta \hat{\mathbf{y}}) d\theta, \quad (2.12)$$

where  $\rho$  is the fluid density. Or equivalently, the forces can be evaluated by the rate of change of total momentum in the fluid. It is conventional to define the lift and drag to be orthogonal and parallel to the velocity at infinity  $u_\infty$ . The dimensionless forces are the lift and drag coefficients:

$$C_d = \frac{F_\perp}{\rho u_\infty^2 c}, \quad C_l = \frac{F_\parallel}{\rho u_\infty^2 c}. \quad (2.13)$$

We will adopt these definitions in our discussion of single-stroke dynamics. However, in the case of flapping, we are interested in the average forces. It is convenient to decompose the forces in the directions corresponding to the mean horizontal flow velocity,  $F_x$  and  $F_y$ . We denote the corresponding dimensionless forces the thrust ( $C_x$ ) and lift ( $C_y$ ) coefficients,

$$C_x = \frac{F_x}{\rho u_1^2 c}, \quad C_y = \frac{F_y}{\rho u_1^2 c}. \quad (2.14)$$

The two sets of definitions are simply choices of reference frames, and have no physical consequences apart from convenience in discussions.

The definition of thrust efficiency is not unique, and we adopt the definition for

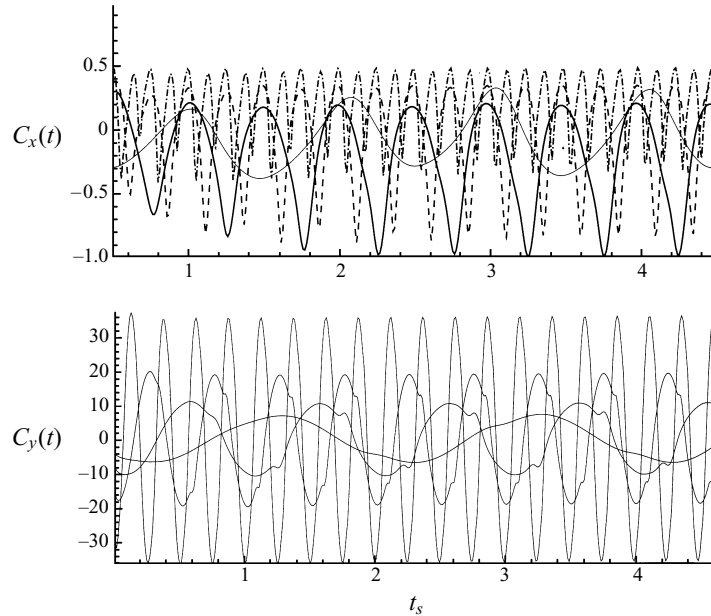


FIGURE 3. Time-dependent thrust and lift coefficients for fixed  $St_a = 0.16$ , and different frequencies,  $f = 0.25, 0.5, 1$ , and  $2$  Hz, or equivalently,  $St_c = 0.5, 1, 2$ , and  $4$ . The frequency of each curve can be read directly from the graph by counting peaks.

the time-averaged thrust efficiency  $Q$  from von Kármán & Bergers (1963), which is reasonable for our model,

$$Q = \frac{\langle F_x(t) \rangle u_0}{\langle F_y(t) u_y(t) \rangle}. \quad (2.15)$$

### 3. Results

First we demonstrate that the optimal flapping frequencies do indeed exist by computing the vortex dynamics and forces around a flapping wing at various frequencies and amplitudes, and later we examine the physical mechanism behind these optima.

We define the optimal flapping to be the one which produces the maximum thrust per unit power input. Among the three parameters, we expect the  $Re$  dependence to be relatively weak for sufficiently high  $Re$ , e.g.  $Re \geq 10^3$ , and fix  $Re$  in our studies. In addition, the parameter  $St_a$  was shown experimentally to be a scaling variable (Triantafyllou *et al.* 1991). We will first fix  $St_a$  and study the dependence of the thrust on various combinations of frequency and amplitude, and later vary  $St_a$ .

#### 3.1. Optimal flapping: observations and qualitative features

In this set of numerical experiments, we set  $Re = 1000$ , and  $St_a = 0.16$ , a number based on forward dragonfly flight with  $f = 40$  Hz,  $A = 2$  cm and  $u = 5$  m s<sup>-1</sup> (Norberg 1975).

Figure 3 shows the thrust and lift coefficients vs. the dimensionless time  $t_s$ , defined as  $t_s = tu_0/c$ , for four different frequencies,  $St_c = 0.5, 1.0, 2.0$  and  $4.0$ . Note we have set  $u_0 = 1$  and  $c = 2$  to fix our units.

---

$St_c$	4	2	1	0.5
$\langle C_x \rangle$	0.18	-0.06	-0.24	-0.08
$\langle C_{xp} \rangle$	-0.02	-0.18	-0.27	-0.12
$\langle C_{xv} \rangle$	0.20	0.12	0.03	0.04
$Q(\%)$	/	1.2	13.5	11.5

---

TABLE 1. Thrust coefficient  $\langle C_x \rangle$  and its two contributions from the pressure force ( $C_{tp}$ ) and the viscous force ( $C_{tv}$ ) as a function of  $St_c$ . Efficiency is calculated only in the cases of positive thrust. The Reynolds number is 1000.

---

The lift coefficients  $C_y$  in the bottom plot vary symmetrically about the zero mean, thus the average vertical force is zero as expected from the symmetric flapping. Little bumps on the three low-frequency curves result from the dynamics of the leading-edge vortices as we shall see in the next figure.

On the other hand, the thrust coefficients  $C_x$  are asymmetric about the zero axis, because the fore-and-aft symmetry is broken by the mean forward velocity field. The frequency of  $C_x$  is twice that of  $C_y$ , because the thrust is generated in both the up and down strokes. By definition, a negative value of  $C_x$  corresponds to a thrust in the mean forward direction. In table 1, we tabulate the average thrust coefficient and the efficiency  $Q$ .  $\langle C_x \rangle$  and  $Q$  reach maxima at  $St_c \sim 1$ .

Next we examine the qualitative features of the associated vortex dynamics in these four cases. First the vortices in the wake rotate in the opposite direction compared to a von Kármán wake. Hence the induced flow has a component moving backward with respect to the wing to generate a thrust (von Kármán & Bergers 1963). As a side remark, the apparent downward drift in both the experiments and these pictures is a transient behaviour due to the initial condition. We check this by repeating the same computation with the initial flap reversed; the small drift is also reversed.

During each period, the trailing-edge vortex begins to shed and grow at the turn of a flap, but the shedding of the leading-edge vortex depends on the angle of attack and the flapping frequency. In figure 4, we compare the vorticity contours for different flapping frequencies at 1/8th of a period. We sketch the basic vortex features next to these figures. In the case of the highest  $St_c$ , the trailing-edge vortex is relatively small, as are the net circulation around the wing and the forces. As  $St_c$  decreases, the trailing-edge vortex grows and the forces increase. Finally, as  $St_c$  further increases, the leading-edge vortex, which has the opposite sign to the trailing-edge vortex starts to shed and reduce the net circulation and the forces. The middle value of  $St_c$  corresponds to the observed optimal thrust and efficiency. To understand these vortex dynamics more quantitatively, we next analyse the growth of vortices and forces in a single stroke.

### 3.2. Single-stroke dynamics

The previous pictures suggest that the following two processes may play significant roles: (1) the unsteady forces due to the trailing-edge vortex growth, similar to the Wagner effect (Wagner 1921), and (2) the shedding of the leading-edge vortex as a function of  $St_c$ . We now investigate these effects in a single stroke moving with velocity  $U$  at an angle of attack  $\alpha$ , which serves as a snapshot of a flapping wing, with  $U$  the sum of  $u_0$  and  $u_1$ ,  $\alpha = \tan^{-1}[u_1(t)/u_0]$ . The lift is defined to be orthogonal to  $U$ , and its forward component corresponds to the instantaneous thrust in the flapping model.



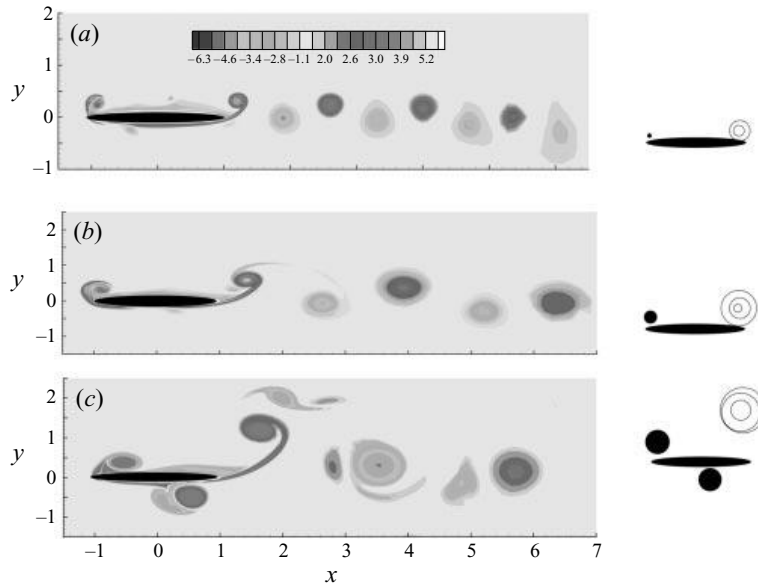


FIGURE 4. Contour plot of the wake vorticity at 1/8th of a period for different frequencies: (a)  $f = 1.0$  ( $St_c = 2.0$ ), (b)  $f = 0.5$  ( $St_c = 1.0$ ), (c)  $f = 0.25$  ( $St_c = 0.5$ ). The grey scale indicates the strength of the vorticity. Other parameters are:  $Re = 1000$  and  $St_a = 0.16$ . The sketches on the right-hand side summarize the basic structure of shed vortices. The leading- and trailing-edge vortices have different signs. In (a), the trailing-edge vortex is small and the leading-edge vortex is bound to the ellipse; in (b), the trailing-edge vortex is larger compared to (a) while the leading-edge vortex is still bound; in (c), both the leading- and trailing-edge vortices are shed (the vortex at the bottom of the ellipse is the leading-edge vortex shed in the previous cycle, which is best viewed in the animation of the simulation.) In the sketches, the black filled dots indicate clockwise-rotating vortices and the circles indicate counter-clockwise-rotating vortices.

### 3.2.1. Unsteady forces

To illustrate the unsteady behaviour, we compute the time-dependent lift on the wing after an impulsive start with an angle of attack  $\alpha$ . We examine the lift coefficient  $C_l$ , as a function of time. Figure 5 shows a case with  $\alpha = 40^\circ$  and  $Re = 1000$ .

The force coefficient curve on the right side of figure 5 shows three different regions. Region A corresponds to the diffusion of the boundary layer vorticity immediately after an impulsive start, and region B corresponds to the roll-up and the growth of the vortex sheet near the tips of the ellipse and the formation of the attached leading-edge vortex. We remark that the transitional point between regions A and B gives a direct measure of the onset of the shedding. Finally, in region C the force settles into a quasi-steady state as the vortices are convected downstream from the body. At a much later time, the leading-edge vortex interacts with the trailing-edge vortex and triggers the onset of the von Kármán wake. The periodicity, however, is on the order of  $T = 10$  as shown in the inset, which is much larger than the time scale of our interest, the flapping period. The relevant time scale for our problem is the characteristic time in region B, which is denoted  $\tau$ , and is on the order of unity. Although the impulsively started flow imposes a special initial condition,  $\tau$  depends mostly on  $Re$  and the geometry of the wing; thus it is expected to be of the same order of magnitude as in more general flows.

A straightforward consequence of the observed unsteady effects is to modify the

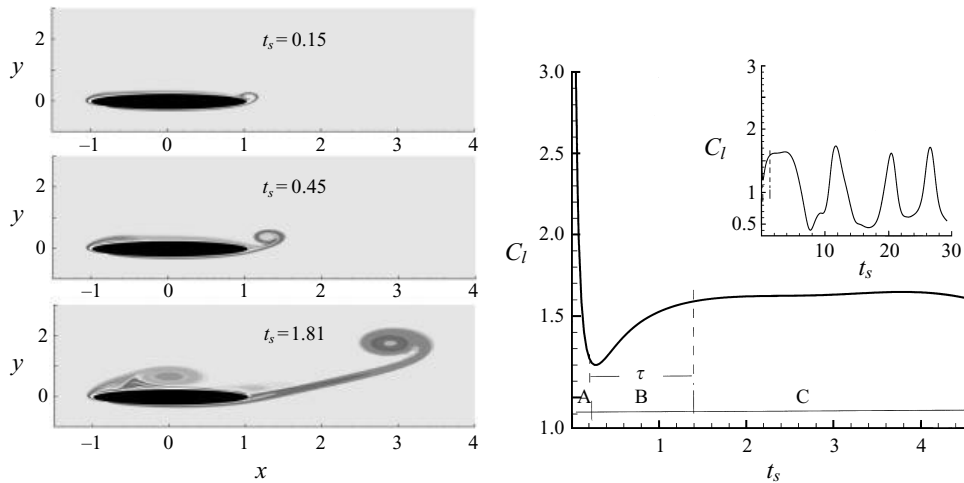


FIGURE 5. Vorticity contour plot (a) and lift coefficient (b) on an impulsively started ellipse with an angle of attack  $40^\circ$ .  $Re = 1000$ . The inset shows the lift coefficient over a longer time period.

forces obtained from the quasi-steady analysis. More interestingly, the unsteady effect also sets an intrinsic time scale  $\tau$  to be compared with the flapping frequency  $St_c$ . Roughly speaking, the wing should flap slowly enough, compared to  $\tau$ , to allow the growth of the vortex. We will return to this point in the next section.

### 3.2.2. Leading-edge vortex

In the previous case with  $\alpha = 40^\circ$ , we note that the leading-edge vortex remains bound to the wing during the time of interest. In this section, we investigate its behaviour as a function of  $\alpha$  and its influence on the lift. In figure 6, we plot the lift coefficient as a function of  $\alpha$  at  $t_s = 2.0$  for  $Re = 192$ . The shape of the curve depends on the time of measurement, as seen in the preceding subsection, and the thickness of the plate, which is illustrated on figure 6(b), where the lift coefficients are shown for two different thickness ratios of the ellipse,  $e = 0.125$  and  $e = 0.25$ . Lift coefficients are higher in the case of a thinner ellipse, which is not surprising. For geometrically similar ellipses subject to the same motion at a fixed Reynolds number, the total lift can only depend on the thickness ratio. In the case of a thinner ellipse, more vortices are shed due to a sharper corner, to result in a higher lift. Consequently we expect that the experimental curve taken by Dickinson & Götz (1993) for a plate, where  $e = 0$ , is higher than the numerics, where  $e = 0.125$ . Nevertheless, the stall angle, corresponding to the maximum lift, appears to be independent of the thickness ratio. This suggests that the stall angle is determined mostly by the Reynolds number, under quasi-steady conditions, for geometrically similar wings. Indeed, the stall angle is found to be around  $45^\circ$  in the experiment and the numerics. The fact that the curve is approximately  $\sin 2\alpha$  suggests that the lift in this case comes from viscous forces.

Early measurements of lift–drag at low Reynolds numbers can also be found in Vogel (1967). To illustrate the  $Re$  dependence of the stall angle, we also include a classical curve for an airfoil, at Reynolds number around  $10^6$  (Prandtl & Tietjens 1934), whose stall angle is about  $12^\circ$ . The larger stall angle at lower Reynolds numbers can be related to the viscous effect that stabilizes the leading-edge vortex. Finally, as a reference, we show the prediction from a two-dimensional potential theory with the

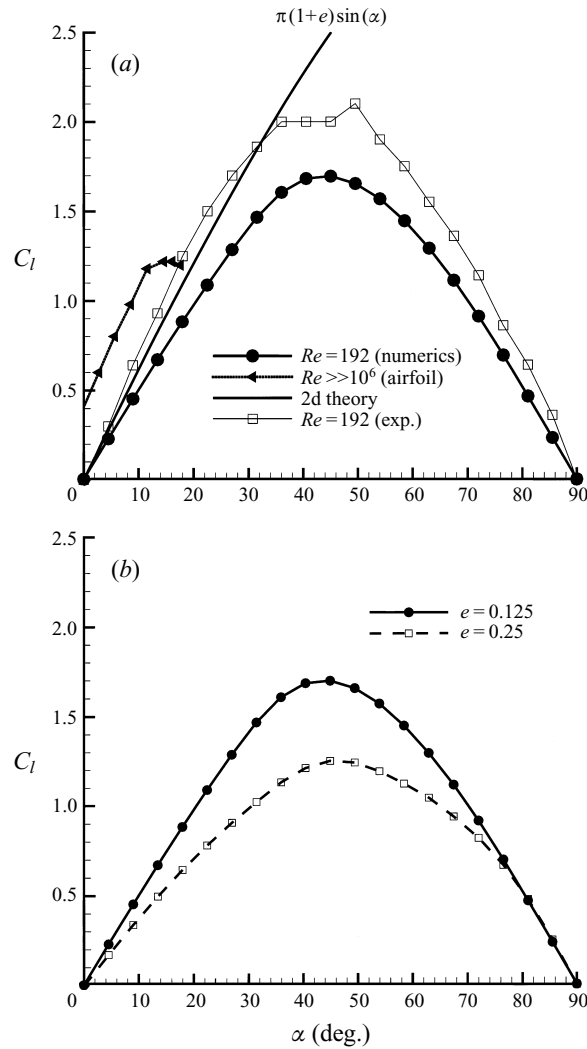


FIGURE 6. (a) Lift coefficient as a function of angle of attack. The experimental curve is taken from figure 4 in Dickinson & Götz (1993). The data are measured at  $t_s = 2.0$ . The classical curve for an airfoil curve is from Prandtl and Tietjens (1934). (b) Lift coefficient as a function of the thickness ratio of the ellipse.

Kutta condition applied to the trailing edge approximated by the tip of the ellipse. Understandably, the classical theory fits the airfoil data with a horizontal shift, to account for the asymmetry, but not the lower Reynolds number flows.

The dynamics of the leading-edge vortex is directly connected to the forces on the wing. At  $Re \sim 1000$ , the lift is dominated by the pressure, which can be expressed by the vorticity flux as

$$P(\theta) = \rho v \int_0^\theta \frac{\partial \omega}{\partial n} ds, \tag{3.1}$$

where  $n$  is the normal vector at the surface, and  $ds$  is the line segment along the

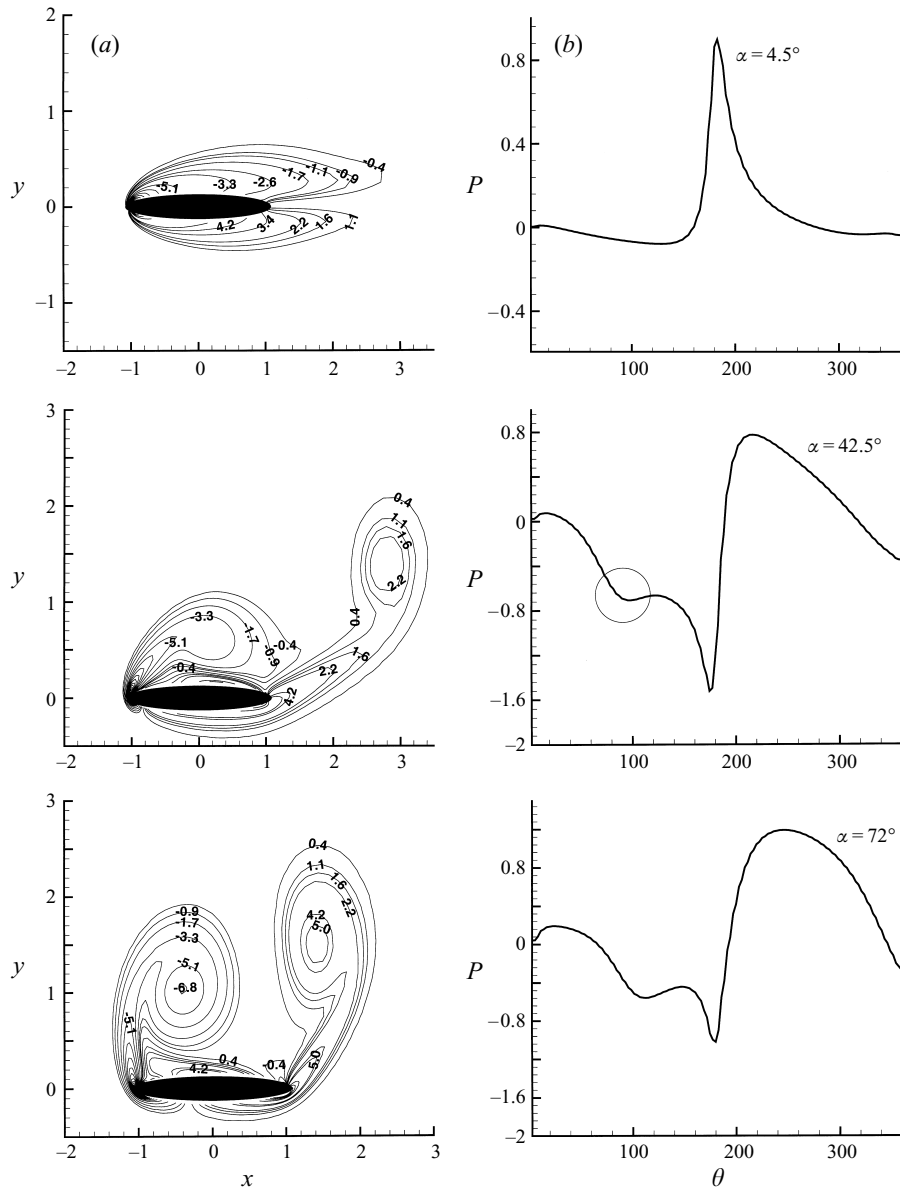


FIGURE 7. Vorticity contours (a) and pressure distribution (b) around a wing for different angle of attack  $\alpha$ .  $\theta = [0, 180^\circ]$  correspond to the upper surface, and  $\theta = [180^\circ, 360^\circ]$  the lower surface.

ellipse, which is parameterized by  $\theta$ . In figure 7 we show the pressure distribution for three typical cases,  $\alpha = 4.5^\circ$ ,  $\alpha = 42.5^\circ$ , and  $\alpha = 72^\circ$  at time  $t = 2.2$ . For each case, we also show the corresponding vorticity configuration. We note that in the cases of the smallest and largest  $\alpha$ , both leading- and trailing-edge vortices are shed, while in the other case, the leading-edge vortex remains bound. The presence of this leading-edge vortex induces a lower pressure region, seen as a dip in the pressure

distribution, which enhances the lift. Although the three-dimensional leading-edge vortex is different, and has a strong component in the axial direction, as seen in the recent work by Ellington (1984), in an early work Savage, Newman & Wong (1978) applied the two-dimensional potential theory to flows around a plate with the presence of a leading-edge vortex at an assumed position, and they found a substantial increase of the force. Our computation can provide a further input to the two-dimensional theory with the position and strength of the leading-edge vortex, governed by the Navier–Stokes dynamics. This provides a basis for our future modelling of these leading-edge vortices.

### 3.3. Optimal flapping: explanations

Now we return to the flapping mode and interpret the observed optimal flapping. In the flapping motion, we are interested in the average thrust. The lift analysed in the previous section has a component in the forward direction which has to overcome the viscous drag in order to generate a net thrust. In figure 8 we show the thrust coefficient of an impulsively started flow at  $Re = 1000$ . The thrust exists only at or above a minimum angle of attack,  $\alpha_{min} = 20^\circ$ , on figure 8(a). More interestingly, both lift and drag are time-dependent, and the thrust only occurs in a time window  $t_s \in (0.2, 1.5)$ , or equivalently,  $t \in (0.4, 3)$ . The lower bound can be associated with the time scale governing the growth of the trailing-edge vortex, hence the lift, as previously seen in figure 5. The upper bound can be attributed to the time scale governing the shedding of the leading-edge vortex which reduces the lift. Each curve, corresponding to a given  $\alpha$ , has a maximum  $|C_x|$ , whose dependence on  $\alpha$  is shown on figure 8(b).

Now we can imagine that during a flapping motion, the effective angle of attack increases from  $0^\circ$  to a maximum angle of attack over time  $T/4$ . In order to achieve a high thrust, there are two conditions. First, as suggested by figure 8, the maximum angle of attack should be in the range of  $45^\circ$ – $60^\circ$  corresponding to  $St_a$  between 0.16 and 0.27, which overlaps with the experimentally observed range (Triantafyllou *et al.* 1991). Secondly, for each fixed  $St_a$ , the wing stroke should be just long enough to stay inside the thrust window. Among the four different frequencies shown in figure 3,  $f = 2$  Hz falls outside the thrust window, and indeed we find a drag instead of a thrust;  $f = 0.5$  Hz corresponds to a situation where the flap just reaches its  $\max(C_x)$  at the end of the half-cycle to benefit from the whole thrust window to produce a large thrust. The other two cases correspond to the intermediate situation.

To confirm this picture, we repeat similar experiments for different  $St_a$ . The results are summarized on figure 9, where the absolute values of the thrust coefficient and efficiency are plotted against  $St_c$ . Note that for each fixed  $St_c$ ,  $|C_x|$  increases with  $St_a$  as expected. Furthermore the maxima occur at  $St_c \sim 0.7$  independent of  $St_a$  at higher  $St_a$ . This is consistent with figure 8, where we observe that the maximum thrust occurs at a time which is insensitive to  $St_a$  for sufficiently high  $St_a$ .

Based on the mechanisms discussed above, we can also speculate on the effect of non-zero mean angle of attack on frequency selection. In particular, in the case of small mean angle of attack and in the limit of linear approximations, the total force is simply rotated from that obtained in the zero mean angle of attack case; thus we expect that the selected frequency remains the same. On the other hand, in the case of large mean angle of attack, the dynamic stall would occur on a smaller time scale, and we expect that the selected frequency would shift toward a slightly higher value. These predictions will be tested in future studies.

In general peaks of efficiency and thrust need not to coincide. Here the efficiency

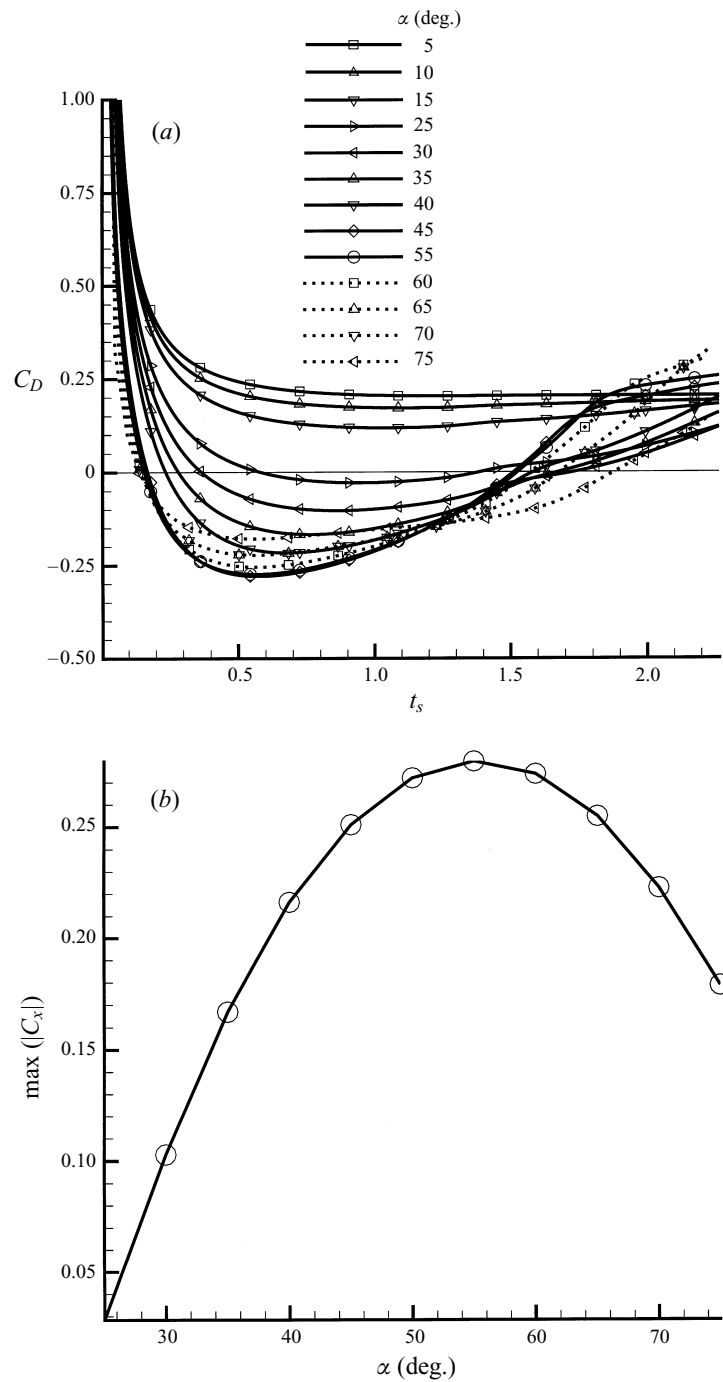


FIGURE 8. Thrust window for different angles of attack. Thrust is the projection of the total force in the mean flow direction.

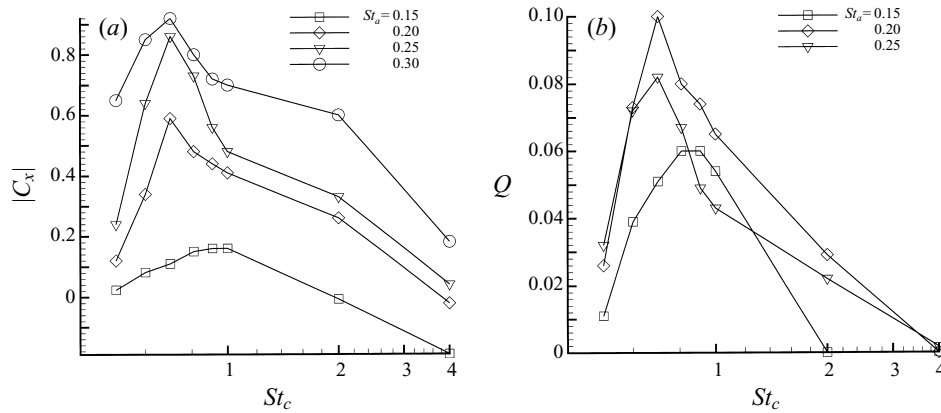


FIGURE 9. Thrust coefficient (a) and efficiency (b) as functions of  $St_c$  for a given  $St_a$ . Different  $St_a$  are represented by different symbols.

shows similar behaviour to the thrust. The low values of thrust indicate that heaving motion alone at low Reynolds numbers is not the best way to generate thrust. Indeed heaving motion is mostly employed by fish, which have much larger Reynolds numbers, and insects typically use the combination of heaving and pitching motions. We will investigate the latter in future work. Nevertheless, we expect that the mechanism for selecting a frequency due to interactions of leading and trailing edges will hold in more complicated motions.

#### 4. Summary

In summary, we implemented and tested a computational tool to resolve the time-dependent vorticity and forces in unsteady viscous flows around a moving wing. We showed an optimal flapping frequency range in a flapping model with two parameters,  $St_a$  and  $St_c$ . By analysing in detail the vortex dynamics and the forces in single strokes, we demonstrated that the preferred  $St_a$  is connected with maximizing the angle of attack allowed for the low range of Reynolds numbers. The optimal flapping frequency,  $St_c$ , for a given  $St_a$ , results from exploiting two intrinsic time scales, one governing the vortex growth and another governing the shedding of the leading-edge vortex. The model studied here only considers the simplest possible flapping motion. In our future studies, more realistic motion which includes both heaving and pitching will be investigated.

It is interesting to note that our observed optimal frequency is very close to the results by Hall *et al.* (1998). This is a curious agreement, considering that the two approaches are rather different. In particular, our wing is two-dimensional, and our approach emphasizes the unsteady effects. On the other hand, their wing is three-dimensional, and each cross-section is treated in the quasi-steady limit with viscous effects incorporated by assuming a quasi-steady lift–drag relation. Their optimal solution essentially determines the load distribution along the spanwise direction. Future work perhaps will show whether the observed agreement is intrinsic or merely accidental.

Animal locomotion is certainly far more complex and diverse than the simple model

considered here. Therefore it is difficult to compare directly the exact numerical values of the observed optimal frequencies with the biological data. Nevertheless, the scaling result shown in figure 9, i.e.  $St_c \sim 0.7$ , suggests that the optimal frequencies are inversely proportional to the dimension of the wing. This is consistent with the data compiled by Greenewalt (1962) in his figures 10 and 12 for birds and insect flight, covering scales of almost three decades, despite the scatter in the data. This apparent agreement does at least encourage one to ask whether the unsteady aerodynamics might guide the selection of frequency in animal flight.

Finally we remark that independent of their possible implications in biological flight, these observed optimal frequencies should be directly of interest to the design of mechanical flapping wings, especially in the light of recent research efforts in micro air vehicles (MAV).

I am grateful to Steve Childress and Mike Shelley for advice and useful discussions, Jianguo Liu for the `ec4` code for cavity flows, David Muraki, and John Wettlaufer for critiques of the manuscript. Finally I thank NERSC for providing the supercomputer CPU time. The work is supported by NSF grant No. DMS-9400912 and DMS-9510356 and DOE grant No. DE-FG02-88ER25053.

### Appendix. Testing the code with impulsively started flows past a cylinder

We test the code in three ways for flow past an impulsively started cylinder. First we find a simple example where the approximate solution to the Navier–Stokes equation is known. Secondly, we compare the computed unsteady velocity field with well-documented experiments by Bouard & Coutanceau (1980). Finally we compute the flow with different resolutions to study its convergence property.

As a first test, we note that after an impulsive start, due to the no-slip boundary condition a thin boundary layer builds up at the surface of the cylinder and diffuses out radially as time increases. The flow outside the boundary layer, however, can still be adequately described by the potential flow:

$$\Psi = -u_0 \left( r - \frac{a^2}{r} \right) \sin \theta, \quad (\text{A } 1)$$

$$u(r) = u_0 \left( 1 - \frac{a^2}{r^2} \right) \cos \theta, \quad (\text{A } 2)$$

$$u_\theta(r) = -u_0 \left( 1 + \frac{a^2}{r^2} \right) \sin \theta, \quad (\text{A } 3)$$

where  $u_0$  is the velocity of the cylinder and  $a$  the radius. We compute at  $Re = 100$  with a resolution  $128 \times 128$ . In figure 10, we plot the azimuthal velocity  $u_\theta(r)$  at  $T = 0.1$  as a function of  $r/a$  with fixed  $\theta = \pi/2$ . The numerical result agrees well with the potential solution outside the boundary layer.

To test the dynamics in the vortex wake, we followed the set up of Bouard & Coutanceau (1980) and computed the velocity field in the wake along the symmetry axis. We compare the time dependent velocity field with the experiments in the case of  $Re = 550$ . The computational grid is  $128 \times 128$ . In figure 10 we copied the experimental points from figure 18 in Bouard & Coutanceau (1980) and overlaid our numerics on top of that. The agreement is remarkably good, considering that the numerics is strictly two-dimensional while the experiment is approximately two-dimensional, and the initial conditions are not exactly the same. In addition, we found



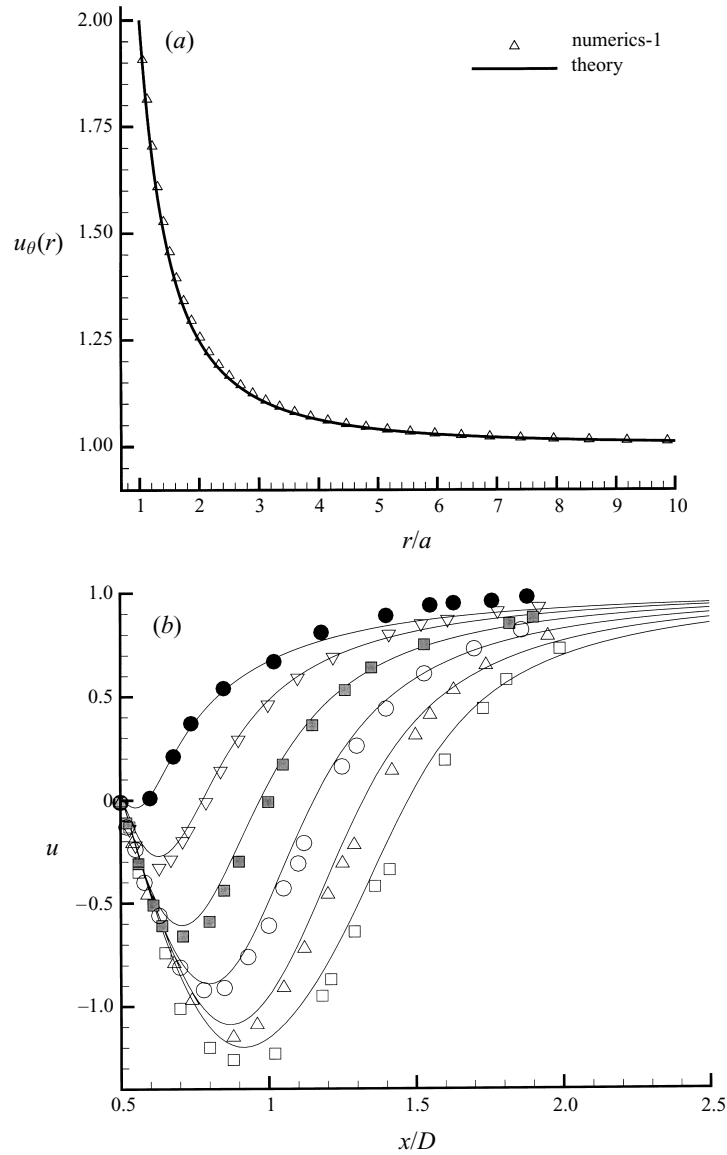


FIGURE 10. (a) Numerical result for azimuthal velocity  $u_\theta(r)$  vs.  $r$  compared with theory. (b) Velocity ( $u$ ) at different locations along the symmetric axis ( $x/D$ ) in the wake, where  $D$  is the diameter of the cylinder. Different symbols correspond to time of measurement (rescaled by  $D/u_0$ ) with an increment of 0.5, starting from  $t_s = 0.5$  (solid circle). Lines are from the numerics, and points are from experiments (Bouard & Coutanceau 1980).

the separation angle at  $Re = 40$  to be  $52.6^\circ$ , which is close to the experimental value,  $53.4^\circ$  (Coutanceau & Bouard 1977).

To further test the convergence of our code, we tested with three different resolutions:  $64 \times 64$ ,  $128 \times 128$ , and  $256 \times 256$ . The time step is fixed to be  $dt = 10^{-4}$ . This small time step is due to the over-resolution in the case of  $256 \times 256$ . We ran the code

for 100 steps, and examined the vorticity along the boundary of the cylinder at the co-located points. In particular, we expected that the ratios  $(\omega_{64} - \omega_{32})/(\omega_{128} - \omega_{64})$  converge to  $2^p$  for the  $p$ th-order method. We found the numerical ratios to be between 16 to 20 along the boundary, consistent with our fourth-order discretization scheme. The convergence study for flow past an ellipse at  $Re = 10000$  was also done in Wang, Liu & Childress (1999).

## REFERENCES

- BOUARD, R. & COUTANCEAU, M. 1980 The early stage of development of the wake behind an impulsively started cylinder for  $40 < Re < 10^4$ . *J. Fluid Mech.* **101**, 583.
- CHILDRESS, S. 1981 *Mechanics of Swimming and Flying*. Cambridge University Press.
- CHOPRA, M. G. 1976 Large amplitude lunate-tail theory of fish locomotion. *J. Fluid Mech.* **74**, 161.
- COUTANCEAU, M. & BOUARD, R. 1977 Experimental determination of the main features of the viscous flow in the wake of a circular cylinder in uniform translation. Part 1. Steady flow. *J. Fluid Mech.* **79**, 231.
- DICKINSON, M. H. & GÖTZ, K. G. 1993 Unsteady aerodynamic performance of model wings at low Reynolds numbers. *J. Exp. Biol.* **174**, 45.
- DICKINSON, M. H., LEHMANN, F. O. & SANE, S. P. 1999 Wing rotation and the aerodynamic basis of insect flight. *Science* **284**, 1954.
- DUDLEY, R. & ELLINGTON, C. P. 1990 Mechanics of forward flight in bumblebees II. Quasi-steady lift and power requirements. *J. Exp. Biol.* **148**, 53.
- E, W. & LIU, J.-G. 1996 Essentially compact schemes for unsteady viscous incompressible flows. *J. Comput. Phys.* **126**, 122.
- ELLINGTON, C. P. 1984 The aerodynamics of hovering insect flight. *Phil. Trans. R. Soc. Lond. B* **305**, 1.
- ELLINGTON, C. P., BERG, C. VAN DEN, WILLMOTT, A. P. & THOMAS, A. L. R. 1996 Leading-edge vortices in insect flight. *Nature* **384**, 626.
- FREYMUTH, P., GUSTAFSON, K. E. & LEBEN, R. 1992 Visualization and computation of hovering mode. In *Vortex Method and Vortex Motion* (ed. K. Gustafson & J. Sethian), p. 143. SIAM, Philadelphia.
- GLAUERT, H. 1929 The force and moment on an oscillating aerofoil. *Tech. Rep. Aero. Res. Comm.* 1242, 742.
- GOPALKRISHNAN, R., TRIANTAFYLLOU, M. S. & TRIANTAFYLLOU, G. S. 1998 Oscillating foils of high propulsive efficiency *J. Fluid Mech.* **360**, 41.
- GUSTAFSON, K. E. & LEBEN, R. 1991 Computation of dragonfly aerodynamics. *Comput. Phys. Commun.* **65**, 121.
- GREENEWALT, C. H. 1962 *Dimensional Relationships for Flying Animals*, vol. 144, no 2, Smithsonian Miscellaneous Collections, Washington DC.
- GURSUL, I. & HO, C.-M. 1992 Oscillating foils of high propulsive efficiency. *AIAA J.* **30**, 1117.
- HALL, K. C., PIGOTT, S. A. & HALL, S. R. 1998 Power requirements for large-amplitude flapping flight. *J. Aircraft* **35**, 352.
- KÁRMÁN VON, F. & BURGERS, J. M. 1963 General aerodynamic theory – perfect fluids. In *Aerodynamic Theory* (ed. W. Durand), vol. 2, Div. E. Springer.
- LIGHTHILL, M. J. 1970 Aquatic animal propulsion of high hydromechanical efficiency. *J. Fluid Mech.* **44**, 265.
- LIGHTHILL, M. J. 1975 *Mathematical Biofluidynamics*. SIAM, Philadelphia.
- LIGHTHILL, M. J. 1977 Introduction to the scaling of aerial locomotion. In *Scaling Effects in Animal Locomotion* (ed. T. Pedley), p. 365. Academic.
- LIU, H., ELLINGTON, C. P., KAWACHI, K., BERG, C. VAN DEN & WILLMOTT, A. P. 1998 A computational fluid dynamics study of hawkmoth hovering. *J. Exp. Biol.* **201**, 461.
- LIU, H. & Kawachi, K. 1998 A numerical study of insect flight *J. Comput. Phys.* **146**, 124.
- MAXWORTHY, T. 1981 The fluid dynamics of insect flight. *Ann. Rev. Fluid Mech.* **13**, 329.
- NORBERG, R. A. 1975 Hovering flight of the dragonfly *Aeschna juncea* L., kinematics and dynamics.

- In *Swimming and Flying in Nature* (ed. T. Y. Wu, C. J. Brokaw & C. Brennen), vol. 2, p. 763. Plenum.
- OSBORNE, M. F. M. 1951 Aerodynamics of flapping flight with application to insects. *J. Expl Biol.* **47**, 561.
- PENNYCUICK, C. J. 1968 On flapping motion of pigeons. *J. Expl Biol.* **49**, 527.
- PHILIPS, P. J., EAST, R. A. & PRATT, N. H. 1981 An unsteady lifting line theory of flapping wings with application to the forward flight of birds. *J. Fluid Mech.* **112**, 321.
- PRANDTL, L. & TIETJENS, O. G. 1934 *Applied Hydro- and Aeromechanics*. McGraw-Hill.
- SAVAGE, S., NEWMAN, B. G. & WONG, D. T.-M. 1979 The role of vortices and unsteady effects during the hovering flight of dragonflies. *J. Expl Biol.* **83**, 59.
- SMITH, M. J. C., WILKIN, P. J. & WILLIAMS, M. H. 1996 The advances of an unsteady method in modeling the aerodynamic forces on rigid flapping wings. *J. Expl Biol.* **199**, 1073.
- SOMPS, C. & LUTTGES, M. W. 1985 Dragonfly flight: Novel uses of unsteady separated flows. *Science* **228**, 1326.
- SPEDDING, G. R. 1992 The aerodynamics of flight. In *Mechanics of Animal Locomotion* (ed. R. M. Alexander), p. 51. Springer.
- SPEDDING, G. R. 1993 On the significance of unsteady effects in the aerodynamic performance of flying animals. *Contemp. Maths* **141**, 401.
- TRIAANTAFYLLOU, M. S., TRIANTAFYLLOU, G. S. & GOPALKRISHNAN, R. 1991 Wake mechanics for thrust generation in oscillation foils. *Phys. Fluids A* **3**, 12.
- TRITTON, D. J. 1992 *Physical Fluid Dynamics*. Oxford.
- VOGEL, S. 1967 Flight in drosophila III. Aerodynamic characteristics of fly wings. *J. Expl Biol.* **46**, 431.
- WAGNER, H. 1921 Über die Entstehung des dynamischen Auftriebes von Tragflüeln. *Z. Angew. Math. Mech.* **5**, 17.
- WAKELING, J. M. & ELLINGTON, C. P. 1997 Dragonfly flight II. Velocities, accelerations and kinematics of flapping flight. *J. Expl Biol.* **200**, 557.
- WANG, Z. J. 1999 Efficient implementation of the exact far field boundary condition for Poisson equation. *J. Comput. Phys.* **153**, 666.
- WANG, Z. J., LIU, J.-G., & CHILDRRESS, S. 1999 Corner vortex and secondary vortices in flow past an ellipse. *Phys. Fluids* **11**, 9.
- WEIS-FOGH, T. & JENSEN, M. 1956 Biology and physics of locust flight. *Proc. R. Soc. B.* **239**, 415–585.
- WEIS-FOGH, T. 1977 Dimensional analysis of hovering flight. In *Scaling Effects in Animal Locomotion* (ed. T. Pedley), p. 405. Academic.
- WU, T. Y. 1977 Introduction to the scaling of aquatic animal locomotion. In *Scaling Effects in Animal Locomotion* (ed. T. Pedley), pp. 203–232. Academic.